Magnetic-field-controlled multitude of spin excitation modes in magnetoelectric $Co_4Nb_2O_9$ as investigated by magnetoterahertz spectroscopy

Rahul Dagar,[1] Satish Yadav,[2] Monu Kinha,[1] Brijesh Singh Mehra,[1] Rajeev Rawat,[2] Kiran Singh,[3,*] and D. S. Rana[1,†]

[1]*Department of Physics, Indian Institute of Science Education and Research Bhopal, Bhopal 462066, Madhya Pradesh, India*

[2]*UGC-DAE Consortium for Scientific Research, University Campus, Khandwa Road, Indore 452001, India*

[3]*Department of Physics, Dr. B. R. Ambedkar National Institute of Technology, Jalandhar 144011, India*

(Received 12 May 2022; revised 4 July 2022; accepted 15 July 2022; published 28 July 2022)

Gapped spin orders induce electric polarization in multiferroics with strong magnetoelectric (ME) coupling. The sensitivity of terahertz (THz) radiation to the spin gaps and the dielectric medium can uniquely access this technologically relevant ME effect. Here, we implement magneto-THz time-domain spectroscopy to demonstrate the manifestation of spin-wave excitations responsible for the ME coupling in multiferroic compound $Co_4Nb_2O_9$. We observed two sharp and a weak spin-gap resonance mode at 0.77, 1.58, and 0.91 THz at 5 K below the antiferromagnetic ordering in the absence of magnetic field. In an applied magnetic field, the strength of the 0.77 THz mode decreases while two field-induced modes, namely, the Goldstone mode and magnon excitation, appear at 0.27 and 1.50 THz, respectively. This THz optical evidence of a rich manifestation of field-controlled magnetic resonances, a mutual transfer of optical spectral weight between the zero-field and field-induced excitations, and associated change of complex refractive index in magnetic fields unravel a unique ME coupling in $Co_4Nb_2O_9$.

DOI: 10.1103/PhysRevMaterials.6.074409

I. INTRODUCTION

Magnetoelectric (ME) materials are of contemporary interest owing to their intriguing physics and technological applications in the field of spintronics, tunable filters, sensors, spin-charge transducers, multistate memories, etc. Cross coupling of both the polarization and magnetization ordered parameters is highly nontrivial in the case of ME materials and can host demanding functionalities for future electronics with less dissipation [1–6]. ME coupling can be achieved via three fundamental processes: (i) in seminal $BiFeO_3$ and its derivative systems, the $6s^2$ lone pair induces ferroelasticity mediated ME coupling, (ii) spin-gapped magnetic order induced ferroelectricity as demonstrated in manganites and some other systems [7–10], and (iii) strain-induced coupling of magnetic and electric order parameters in composite heterostructures [11]. However, there exist other types of ME materials which exhibit dielectric anomaly and ferroelectricity only in the presence of a magnetic field [1,12–14]. While such external control is a very technologically relevant aspect of the ME effect, the understanding of the evolution of magnetic order and its coupling to electric dipoles leaves much to be desired.

$Co_4Nb_2O_9$ (CNO) is a contemporary ME material which belongs to the family of isostructural compounds having a general formula $Me_4A_2O_9$ (Me = Co, Mn, Fe, Mg; A = Nb, Ta) and crystallizes in α-Al_2O_3 type trigonal centrosymmetric crystal structure (space group $P\bar{3}c1$) [15–17]. The crystal structure of CNO is shown in the Supplemental Material (see Sec. S1 [18]). CNO exhibits antiferromagnetic (AFM) order with a simultaneous transition to a ME phase at ∼27 K (T_N) [15]. An anomaly in the dielectric constant at T_N in a magnetic field >12 kOe was attributed to a magnetically driven spin-flop phase transition [14] and is understood to be a consequence of both the spin rotations and magnetic domain alignment [19]. A few studies using neutron diffraction, albeit with some contradictions, have contributed to the understanding of the complex magnetic structure of this system [20–23]. In a magnetic order driven ME system, such as CNO, the gapped nature of the spin order induces and couples with the electric order. A magnetic-field dependence of the spin-wave modes/gaps with a possibility of new modes and resultant evolution of dielectric medium are key factors to understanding the nature of the ME character of this compound.

Terahertz (THz) spectroscopy is a contemporary tool which is uniquely sensitive to both AFM-order-based excitations and dielectric medium of the ferroelectric order. Both these indispensable attributes can unravel the field-induced emergent magnetic excitations responsible for the ME coupling in CNO. In addition, THz has also been used efficiently to probe other low-energy-gapped phenomenon such as charge-density waves, superconducting gaps, low-lying phonon modes, inter- and intralevel excitations, etc. [24–30], and recently emerged as a fulcrum of ultrafast optical control in AFM spintronics. Here, we employ THz time-domain spectroscopy as a function of temperature in the range of 2–300 K and in a magnetic field up to 5 T on ME CNO. We observed three high-frequency zero-field magnetic resonance modes at 0.77 THz (m_1), 1.58 THz (m_2), and 0.91 THz (m_3) at 5 K, and two magnetic-field-induced modes at 0.27 (m_4) and 1.50 (m_5)

*singhkp@nitj.ac.in
†dsrana@iiserb.ac.in

THz. Weakening or disappearance of the zero-field modes in a magnetic field at the expense of strengthening of the field-induced modes in high magnetic fields unveils a unique field control of multiple spin gaps and spin reorientation. These unique features along with a field-controlled complex refractive index are the ingredients of the ME coupling in CNO.

II. EXPERIMENTAL DETAILS

A polycrystalline bulk sample of CNO was prepared using the standard solid-state reaction route using Co_3O_4 and Nb_2O_5 as the starting reactants. Both stoichiometric powders were ground thoroughly using a mortar and pestle and then calcinated for 6 h at 1000 °C. After calcination, the bulk sample was again reground for 6 h and pressed to make pellets of 8 mm diameter with thickness of around 0.65 mm and sintered for 6 h at 1100 °C. The detailed sample synthesis and structural characterization has been provided elsewhere [31]. We have used the bulk sample from the same batch for the measurements as by Yadav *et al.* [31]. The high-resolution synchrotron radiation diffraction (SXRD) measurement is also performed at angle dispersive x-ray diffraction beamline (BL-12) [32] at Indus-2, RRCAT Indore ($\lambda = 0.75253$ Å). The data conversion is made using FIT2D software [33]. The SXRD data are refined using FULLPROF software [34]. Magnetic measurements were performed in the temperature range of 1.8–300 K on a superconducting quantum interference device [SQUID VSM (Quantum Design)]. THz time-domain spectroscopy (TDS) was implemented in transmission mode in the temperature range from 2 to 300 K and magnetic field from 0 to 5 T. More detailed information about the setup is provided in the Supplemental Material (see Sec. S2 [18]).

Here, in the measurements we have averaged out 5000 single-shot pulses to improve the signal-to-noise (SNR) ratio. To further enhance SNR and diminish unwanted absorption of THz pulses by water [35], the measurements were performed in dry nitrogen atmosphere. THz measurements were performed in Faraday geometry in which the external magnetic field is perpendicular to the surface of the polycrystalline bulk sample. The optical coefficients such as refractive index and the absorption coefficient of the material were obtained as follows: First, we passed the temporal THz pulse through the free space (cryo) at a given temperature, and the magnetic field, which served the purpose of being a reference. After collecting the transmitted THz pulse through the reference, the THz pulse was then passed through the sample under the same identical condition as that for the reference. The fast Fourier transformation (FFT) of the transmitted THz pulse gives the information of the phase and amplitude in the frequency domain. From this FFT data, we can extract the information about the optical coefficients of the sample.

III. STRUCTURAL CHARACTERIZATION

The Rietveld refined room temperature SXRD pattern is presented in Fig. 1. All the peaks are well refined with the $P\bar{3}c1$ space group. There is no additional peak which is not fitted with the $P\bar{3}c1$ space group which corroborates the absence of any impurity phase within the instrument resolution. This confirms the phase purity of the prepared samples. The refined lattice parameters are $a = b = 5.1709$ (2) Å and $c = 14.1367$ (7) Å. This is consistent with earlier reports [14,15,31]. The red circles represent the experimental data and the black line represents the calculated diffraction. The vertical green lines correspond to Bragg's peaks and the blue line at the bottom is the difference between the experimental and calculated diffraction patterns. The SXRD data confirm the single phase of the prepared samples.

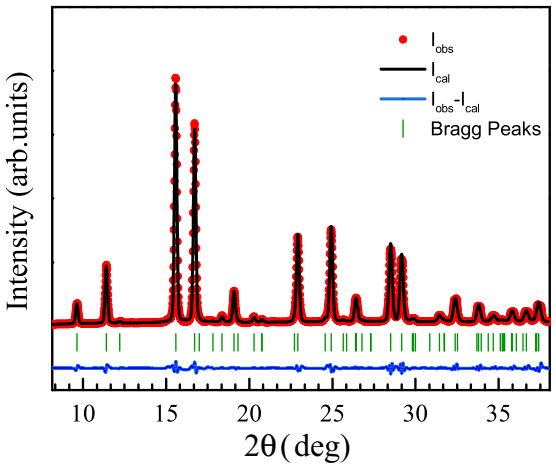

FIG. 1. Rietveld refinement of room temperature SXRD pattern.

IV. TEMPERATURE DEPENDENT THz-TDS MEASUREMENTS

Figure 2(a) shows the absorption coefficient (α) in the THz frequency region at different temperatures above and below the T_N in zero magnetic field. Here, the absorption spectra were normalized with transmission data at 60 K where the spectrum is devoid of any sharp or subtle resonance feature. Two sharp resonance absorption lines were observed at frequencies of 0.77 and 1.58 THz at 5 K. These modes (m_1 and m_2) weaken and broaden with increasing temperature and completely diminish on approaching the T_N, which clearly suggests their origin in the gapped AFM resonance. In addition to these two sharp absorption lines, a weak resonance absorption (m_3) was also observed at low temperatures. While the m_1 is nearly coincident with a gapped mode at ~3.1 meV observed by inelastic neutron scattering measurements [23], the m_2 and m_3 modes are an observation which is suggestive of the presence of multiple gaps.

In order to explore the behavior of mode m_1 with respect to temperature, the peak position of m_1 is plotted at different temperatures [see inset of Fig. 2(a)]. Upon increasing temperature from 2 K, the intensity of the m_1 mode increases while mode frequency remains unchanged. At around 10 K, the intensity of mode m_1 reaches the maximum and gets blueshifts with increasing temperature which suggests the temperature-induced phase transition in CNO at around 10 K [36]. This blueshift of the m_1 mode with increasing temperature is a rare observation in AFM materials. In a THz spectroscopy study on NiO, the AFM resonance mode gets redshifted which was attributed to

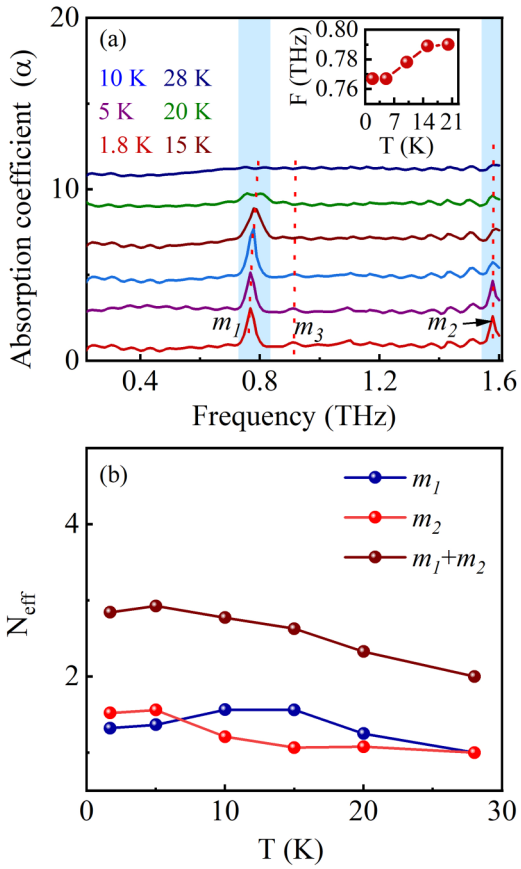

FIG. 2. (a) Absorption coefficient versus frequency at different temperatures, after normalizing to the 60 K absorption spectrum. Here, the spectrum is translated along the y axis to clearly show the resonance absorptions. The corresponding inset shows the peak position of mode m_1 as a function of temperature. (b) Total spectral weight (N_{eff}) of m_1, m_2, and $m_1 + m_2$ modes as a function of temperature after being normalized with respect to 28 K.

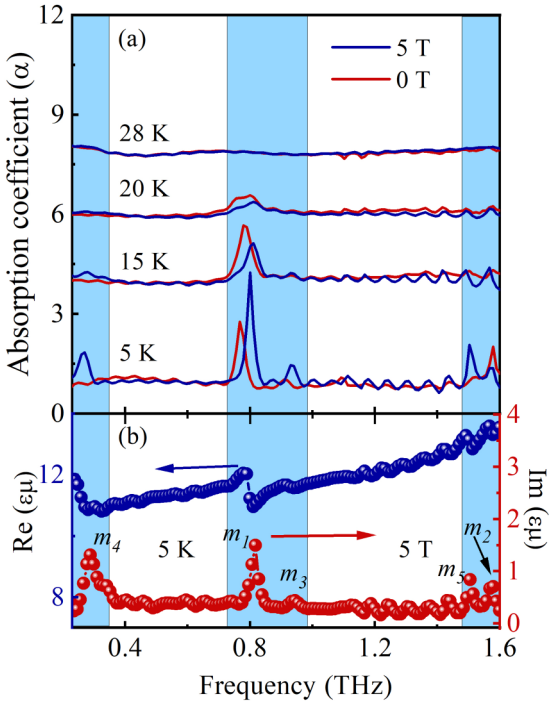

FIG. 3. (a) Normalized absorption coefficient versus frequency in the presence of magnetic fields of strength 0 and 5 T at temperatures of 5, 15, 20, and 28 K, and (b) the real Re ($\varepsilon\mu$) and imaginary Im ($\varepsilon\mu$) as a function of frequency in the presence of magnetic field of strength 5 T at 5 K. Shaded area in (a), (b) shows the resonance modes. Blue and red arrows in the bottom panel correspond to left and right y axis, respectively.

an increase in the spontaneous magnetization of the magnetic sublattice [37]. Redshift of the imaginary Im ($\varepsilon\mu$) was observed in $Gd_{0.7}Tb_{0.3}MnO_3$ with increasing temperature [38]. The redshift of both quasi-FM and quasi-AFM modes was recently observed with temperature in rare-earth orthoferrite systems [39].

To gain more insight about the origin of the resonance mode in the present case, the integrated spectral weight (N_{eff}) per Co site was calculated at different temperatures using the following relation,

$$N_{\text{eff}} = \left(\frac{2m_0V}{\pi e^2}\right)\int_{\omega_1}^{\omega_2} \omega\ \text{Im}\ (\varepsilon\mu)d\omega, \qquad (1)$$

where m_0, e, V, ε, and μ are the free electron mass, electronic charge, unit cell volume, electric permittivity, and magnetic permeability, respectively [38,40]. Here, ω_1 and ω_2 were chosen as 0.74 and 0.85 THz for the m_1 mode and 1.56 and 1.60 THz for the m_2 mode to cover the entire resonant absorptions. As seen in Fig. 2(b), on decreasing the temperature below T_N, the N_{eff} increases which is again reminiscent of the magnetic origin of mode m_1. Furthermore, the N_{eff} shows an unusual trend around 10 K; it peaks at this temperature and decreases below it. This behavior is coincident with the appearance of a second zero-field mode at 1.58 THz. The loss of spectral weight in mode m_1 below 10 K is transferred to the mode m_2 manifesting at 1.58 THz [see Fig. 2(b)]. As these modes are associated with the AFM order, this transfer of spectral weight between the two modes suggests the spin reorientation effect which is a unique observation in such ME systems. This is also corroborated by the bulk magnetization (M) versus temperature (T) data (Fig. S3 in the Supplemental Material [18]). As the M versus T data suggested only a dominant 27.2 K Néel's transition, it is the dM/dT plot which shows two points of inflection at 10 and 27.2 K. The 10 K feature is relatively subtle to be interpreted from M versus T data (Fig. S3(b) [18]). However, it depicts a discernible change in the magnetization profile which translates into a pronounced THz response in terms of manifestation of the m_2 mode associated with it, as elaborated upon above.

V. MAGNETIC FIELD DEPENDENT THz TDS MEASUREMENTS

Since CNO is a magnetic-field-induced ME material, it necessitates the understanding of the dynamics of the gapped mode and the possibility of more resonance excitation enriching the ME character in the presence of magnetic field. Low-energy excitations such as electromagnons and AFM spin-wave excitations have been previously observed in ME materials because of the simultaneous coupling of both ordered parameters via spin-orbit interaction. These excitations

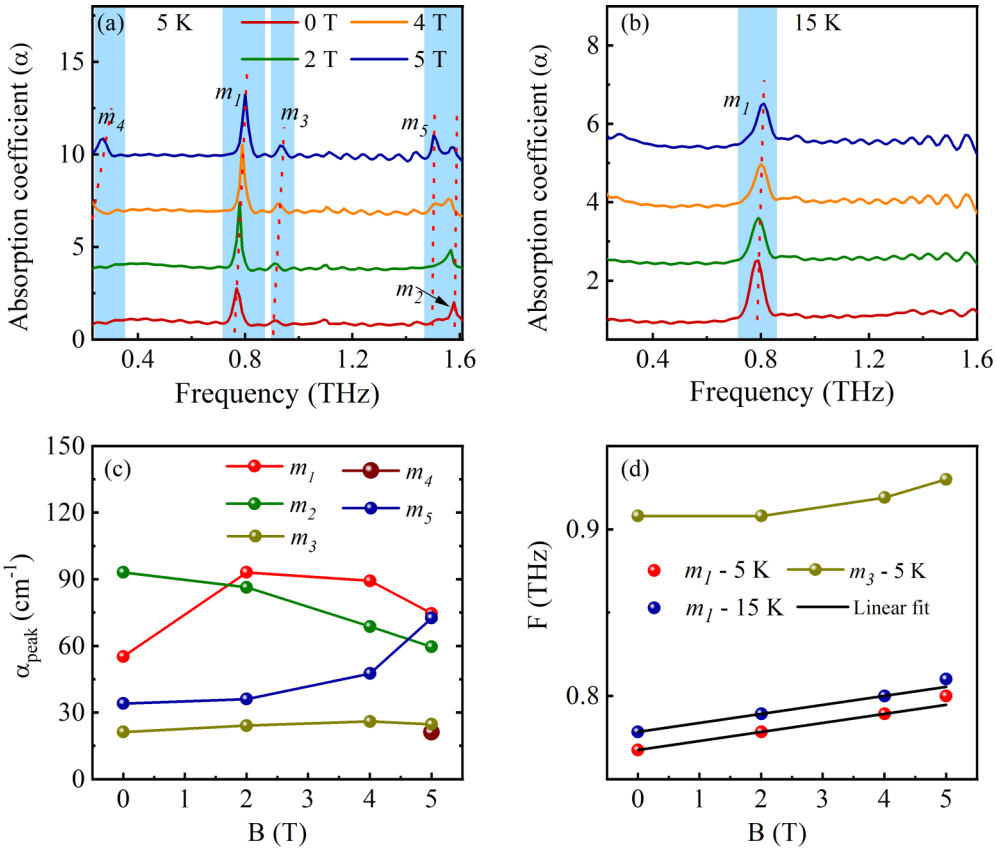

FIG. 4. (a), (b) Absorption coefficient versus frequency in the presence of magnetic fields of various strengths at 5 and 15 K, after normalizing with 60 K at the same magnetic field. Here, the spectrum is translated along the *y* axis. (c) The maxima of absorption coefficient (α_{peak}) of modes (m_1–m_5) as a function of magnetic field at 5 K. (d) Peak position of resonance mode centered at 0.77 and 0.91 THz as a function of magnetic field at 5 and 15 K. Here, lines joining the data points are guides to the eye and the black line shows the linear fit.

could be either electric dipole active magnetic resonances or spin-wave excitation which is driven by the magnetic component [38]; however, both types of such resonance underline the ME behavior.

Figures 3 and 4 show detailed magnetic field (H) dependent THz spectra at different temperatures. Clearly, two modes, m_4 and m_5, emerge in applied magnetic fields, making a multitude of five magnetic modes. A dielectric dispersion for all 0.27 THz (m_4), 0.8 THz (m_1), 0.91 THz (m_3), 1.50 (m_5) THz, and 1.58 (m_2) THz at 5 K modes in the presence of $H =$ 5 T confirms them as resonance excitations [Fig. 3(b)]. At 5 K the m_1 strengthens in a magnetic field of up to 2 T but weakens on further increasing the field [see Figs. 4(a) and 4(c)]. The weakening is accompanied by strengthening of mode m_3 on an application of a magnetic field of 2 T and above. The peak position of m_1 shifts linearly up to 4 T while it is nonlinear for m_3 [see Fig. 4(d)]. The linear dependency of m_1 could be related with the robustness of the AFM phase up to 4 T, while a slight deviation in $H > 4$ T could be related to the emergence of a field-induced small ferromagnetic component [19]. Incidentally, two additional field-induced modes m_4 and m_5 appear at critical H of 5 and 2 T, respectively [see Figs. 4(a) and 4(c)]. The mode m_4 appears from the low-frequency side and blueshifts as the applied field increases beyond 4 T. Here, the emergence of m_4 can be attributed to a gapless Goldstone mode in the zero-field limit [23]. The magnetic-field-induced Goldstone mode has been previously reported in tetragonal crystal structure compound $Ba_2CoGe_2O_7$ [41,42]. In contrast, the field-induced mode m_5 shows no shift with increasing field and increases with increasing magnetic field which we speculate to be a magnetic excitation. To gain further insight about these resonance modes, the maxima of the absorption coefficient [see Fig. 4(c)] and the spectral weight (see Fig. S6 [18]) of these resonance modes at 5 K were plotted as a function of magnetic field which suggested that there is a spectral weight transfer from the zero-field-induced modes to that of field-induced modes.

As depicted in a previous section, there is a transfer of spectral weight from a zero-field mode to a field-induced mode. The Co ion in this system is in a high-spin state [19]. Nb^{5+} being in a fully filled state rules out the possibility of any magnetic exchange interactions of Co with Nb ions. Further, a nonmonotonic field dependence (blueshifting) of mode m_4 and a linear dependence of mode m_5 (no shifting) [Fig. 4(a)] in the applied field confirms the unique dynamics of the magnetic excitations. We further note that the field dependent behavior of mode m_1 at 15 K is different from that at 5 K. At 15 K, this mode suppresses monotonically with increasing magnetic field [see Fig. 4(b)]. This difference is presumably due to the spin reorientation that sets in at 10 K and which is also reflected in the dynamic transfer of the spectral weight between the m_1 and m_2 modes [Fig. 2(b)]. Besides, the

modes at 1.58 THz appear below 10 K and strengthen with decreasing temperature and weaken with increasing magnetic field [see Figs. 2(a), 4(a), and 4(c)]. Overall, it is surmised that the field-induced modes (m_4 and m_5) grow at the expense of the zero-field modes (m_1, m_2, and m_3) (see Fig. S6 [18]).

A similar observation in a zero-field ME $TbMnO_3$ was assigned to the dynamics between an electromagnon and a magnon at a higher magnetic field and was attributed to destabilizing the spin structure on the application of a magnetic field [26]. However, in the present case, CNO exhibits a large in-plane magnetic anisotropy compared to the dominant magnetic interaction [23]. In such cases, both neighboring spins S_i and S_j lie in plane even upon application of a magnetic field normal to the plane. Understanding this in the context of the spin current model [$P \sim e_{ij} \times (S_i \times S_j)$, where e_{ij} is a unit vector connecting S_i and S_j], the net polarization is zero in the absence of magnetic field due to antiparallel spin configurations. In applied fields, the magnetic moment will slightly rotate in the direction of the field to minimize the angle with the external field, yielding a net nonzero electric polarization [23]. This hybrid spin lattice excitation or spin polarization excitation holds generic relevance in the present case and could be responsible for these magnetic excitations present in the CNO on the application of a magnetic field.

Further, Fresnel's equations were used to extract the THz dielectric constant from the complex refractive index, as explained elsewhere [43]. As such the refractive index $n(\omega)$ should be expressed as $n(\omega) = \sqrt{\varepsilon(\omega)\mu(\omega)}$, where $\varepsilon(\omega)$ and $\mu(\omega)$ are the electric permittivity and magnetic permeability, respectively. Figure 5(a) shows the real part Re $(\varepsilon\mu)$ of the complex refractive index as a function of temperature in the absence and presence of a magnetic field of 5 T at a fixed frequency of 0.5 THz. The Re $(\varepsilon\mu)$ is nearly constant in the range of room temperature to T_N while it shows a subtle increase below T_N to 5 K. Since, far from the resonance excitations, i.e., above T_N, the response is pure dielectric, therefore, the Re $(\varepsilon\mu)$ can be interpreted as the real part of the dielectric constant above T_N. This observed behavior of the dielectric constant above T_N to room temperature is different from the earlier reports where the measurements were performed in the kHz to MHz frequency regime [14,44]. This difference in the dielectric constant behavior in the THz frequency regime can be attributed to the relaxation of orientation polarization [44]. To understand the effect of a magnetic field on the dielectric constant, Re $(\varepsilon\mu)$ was calculated in the presence of various magnetic fields at 0.5 THz. The inset of Fig. 5(a) shows the Re $(\varepsilon\mu)$ as a function of magnetic field at different temperatures at 0.5 THz. The Re $(\varepsilon\mu)$ decreases with magnetic field below T_N; it is constant at all magnetic fields above this temperature. Figures 5(b) and 5(c) show the transmitted THz pulse from the CNO polycrystalline bulk sample at 5 and 28 K, respectively. At 5 K, the THz pulse arrives early at higher magnetic fields implying a decrease in THz refractive index on the application of a magnetic field [45]. Above T_N at 28 K, the effect of the magnetic field on the THz waveform is negligible which suggests that the ME coupling ceases to manifest above T_N [see Fig. 5(c)].

THz AFM spintronics has various facets in its rapidly expanding materials base. Transition metal oxides, the fulcrum of this emerging area, have hosted two types of effects,

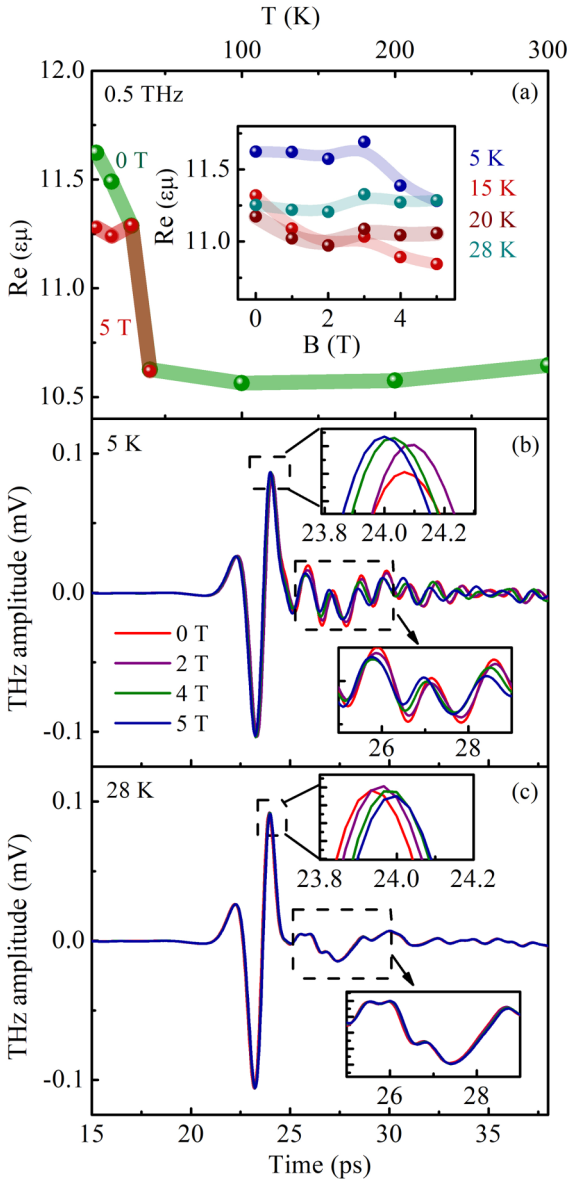

FIG. 5. (a) Real Re $(\varepsilon\mu)$ as a function of temperature in the absence and presence of magnetic field of 5 T at 0.5 THz. The corresponding inset shows real Re $(\varepsilon\mu)$ as a function of magnetic field at temperature of 5, 15, 20, and 28 K; (b), (c) show transmitted THz pulse through the CNO polycrystalline sample in the presence of different magnetic fields at 5 and 28 K, respectively. Corresponding insets in (b), (c) show the magnified waveform for better viewing.

namely, THz emission by AFM order and THz control of AFM resonant modes. While THz AFM resonances and their optical control were demonstrated in NiO [28,37,46], rich dynamics of interaction between THz radiation and AFM order manifested in orthoferrites [47–49]. Observation of magnons and electromagnons in multiferroic manganites [38,50] and some other oxides further depicted the THz optical control of the ferroelectric order and the ME coupling [51,52]. Another notable study unveiled the chirality in a square-lattice antiferromagnet via spin excitation probed by magneto-THz data [41]. A number of bound magnon states have been reported in quantum AFMs [53,54]. Compared to these reports, the

present CNO system belongs to a different class of field-induced ME systems. The magneto-THz studies presented here add a dimension to the AFM spintronics as well as contribute to the understanding of its ME character. In the former context, observation of the zero-field and magnetic-field-induced AFM resonances and dynamic shifting of the spectral weight between the two depicts THz controls of magnetic-field-induced spin reorientation of the AFM order. For the latter case, field-induced suppression/blueshift of zero-field modes with simultaneous field-induced emergent modes in conjunction with change in refractive index in a magnetic field unveil the following: (i) as per the spin current model, the magnetic moments rotate in the direction of the field and yield a net nonzero electric polarization; (ii) field-induced spin gaps/modes associated with the change in refractive index are a unique effect not only in CNO but in the entire range of ME systems.

VI. CONCLUSION

To sum up, the demonstrated implementation of magneto-THz spectroscopy on ME material CNO unravels a rare multitude of five zero-field and field-induced spin excitation modes in a ME system. Field-induced shifting of spectral weight between the two types of field-controlled modes along with a change of refractive index in the magnetic field corroborate and depict the uniqueness of ME coupling in CNO. While THz spin excitations in some AFM systems have created a niche to control the AFM order, THz optical control of spin excitations of the nonlinear ME AFM medium, as demonstrated in this study, has further implications in the mutual control of two orders of a ME system. This experimental framework can potentially inspire studies on low-energy optical control of magnetic-order-driven ME effect in a range of technologically relevant multiferroic systems.

All data needed to evaluate the conclusions in the paper are present in the paper and its Supplemental Material [18].

ACKNOWLEDGMENTS

D.S.R. thanks the Science and Engineering Research Board (SERB), Department of Science and Technology, New Delhi, for financial support under research Project No. CRG/2020/002338. K.S. also thanks SERB for financial support under research Project No. CRG/2021/007075. K.S. and R.R. thank Dr. A. K. Sinha and Mr. M. N. Singh for their support for room temperature SXRD measurements.

[1] W. Eerenstein, N. D. Mathur, and J. F. Scott, Nature (London) **442**, 759 (2006).
[2] F. Matsukura, Y. Tokura, and H. Ohno, Nat. Nanotechnol. **10**, 209 (2015).
[3] H. Schmid, Ferroelectric **162**, 317 (1994).
[4] S.-W. Cheong and M. Mostovoy, Nat. Mater. **6**, 13 (2007).
[5] T. Kimura, Annu. Rev. Mater. Res. **37**, 387 (2007).
[6] R. Ramesh and N. A. Spaldin, Nat. Mater. **6**, 21 (2007).
[7] T. Kimura, T. Goto, H. Shintani, K. Ishizaka, T. Arima, and Y. Tokura, Nature (London) **426**, 55 (2003).
[8] T. Kimura, Y. Sekio, H. Nakamura, T. Siegrist, and A. P. Ramirez, Nat. Mater. **7**, 291 (2008).
[9] T. Hur, S. Park, P. A. Sharma, J. S. Ahn, S. Guha, and S.-W. Cheong, Nature (London) **429**, 392 (2004).
[10] K. Singh, C. Simon, E. Cannuccia, M.-B. Lepetit, B. Corraze, E. Janod, and L. Cario, Phys. Rev. Lett. **113**, 137602 (2014).
[11] C.-W. Nan, L. Liu, N. Cai, J. Zhai, Y. Ye, Y. H. Lin, L. J. Dong, and C. X. Xiong, Appl. Phys. Lett. **81**, 3831 (2002).
[12] N. Mufti, G. R. Blake, M. Mostovoy, S. Riyadi, A. A. Nugroho, and T. T. M. Palstra, Phys. Rev. B **83**, 104416 (2011).
[13] J. Hwang, E. S. Choi, H. D. Zhou, J. Lu, and P. Schlottmann, Phys. Rev. B **85**, 024415 (2012).
[14] T. Kolodiazhnyi, H. Shakurai, and N. Vittayakorn, Appl. Phys. Lett. **99**, 132906 (2011).
[15] Y. Fang, Y. Q. Song, W. P. Zhou, R. Zhao, R. J. Tang, H. Yang, L. Y. Lv, S. G. Yang, D. H. Wang, and Y. W. Du, Sci. Rep. **4**, 3860 (2014).
[16] N. D. Khanh, N. Abe, K. Matsuura, H. Sagayama, Y. Tokunaga, and T. Arima, Appl. Phys. Lett. **114**, 102905 (2019).
[17] K. Momma and F. Izumi, J. Appl. Cryst. **44**, 1272 (2011).
[18] See Supplemental Material at http://link.aps.org/supplemental/10.1103/PhysRevMaterials.6.074409 for the crystal structure, magnetic characterization, temperature and magnetic field dependent absorption coefficient, and magnetic field dependent spectral weight of polycrystalline $Co_4Nb_2O_9$ sample.
[19] L. Ding, M. Lee, T. Hong, Z. Dun, R. Sinclair, S. Chi, H. K. Agrawal, E. S. Choi, B. C. Chakoumakos, H. Zhou, and H. Cao, Phys. Rev. B **102**, 174443 (2020).
[20] E. F. Bertaut, L. Corliss, F. Forrat, R. Aleonard, and R. Pauthenet, J. Phys. Chem. Solids **21**, 234 (1961).
[21] B. Schwarz, D. Kraft, R. Theissmann, and H. Ehrenberg, J. Magn. Magn. Mater. **322**, L1 (2010).
[22] N. D. Khanh, N. Abe, H. Sagayama, A. Nakao, T. Hanashima, R. Kiyanagi, Y. Tokunaga, and T. Arima, Phys. Rev. B **93**, 075117 (2016).
[23] G. Deng, Y. Cao, W. Ren, S. Cao, A. J. Studer, N. Gauthier, M. Kenzelmann, G. Davidson, K. C. Rule, J. S. Gardner, P. Imperia, C. Ulrich, and G. J. McIntyre, Phys. Rev. B **97**, 085154 (2018).
[24] K. S. Kumar, G. L. Prajapati, R. Dagar, M. Vagadia, D. S. Rana, and M. Tonouchi, Adv. Opt. Mater. **8**, 1900958 (2020).
[25] D. S. Rana and M. Tonouchi, Adv. Opt. Mater. **8**, 1900892 (2020).
[26] P. Rovillain, M. Cazayous, Y. Gallais, M-A. Measson, A. Sacuto, H. Sakata, and M. Mochizuki, Phys. Rev. Lett. **107**, 027202 (2011).
[27] T. Kampfrath, K. Tanaka, and K. A. Nelson, Nat. Photon. **7**, 680 (2013).
[28] T. Kampfrath, A. Sell, G. Klatt, A. Pashkin, S. Mährlein, T. Dekorsy, M. Wolf, M. Fiebig, A. Leitenstorfer, and R. Huber, Nat. Photon. **5**, 31 (2011).
[29] A. Pimenov, A. Shuvaev, A. Loidl, F. Schrettle, A. A. Mukhin, V. D. Travkin, V. Yu. Ivanov, and A. M. Balbashov, Phys. Rev. Lett. **102**, 107203 (2009).
[30] R. Dagar, M. Kinha, and D. S. Rana, Europhys. Lett. **138**, 66002 (2022).

[31] S. Yadav, M. Chandra, and K. Singh, Ceram. Int. **45**, 12022 (2019).
[32] A. K. Sinha, A. Sagdeo, P. Gupta, A. Upadhyay, A. Kumar, M. N. Singh, R. K. Gupta, S. R. Kane, A. Verma, and S. K. Deb, J. Phys.: Conf. Ser. **425**, 072017 (2013).
[33] A. P. Hammersley, S. O. Svensson, and A. Thompson, Nucl. Instrum. Methods Phys. Res. Sect. A **346**, 312 (1994).
[34] J. Rodríguez-Carvajal, Physica B **192**, 55 (1993).
[35] H. Cui, X. Zhang, J. Su, X. Wei, Y. Guo, Q. Fang, and Y. Yang, in *International Photonics and Optoelectronics Meetings, OSA Technical Digest* (online) (Optica Publishing Group, 2014), paper OF5A.8.
[36] L. Y. Shi, X. M. Wang, R. D. Zhong, Z. X. Wang, T. C. Hu, S. J. Zhang, Q. M. Liu, T. Dong, F. Wang, and N. L. Wang, Phys. Rev. B **104**, 144408 (2021).
[37] Z. Wang, S. Kovalev, N. Awari, M. Chen, S. Germanskiy, B. Green, J.-C. Deinert, T. Kampfrath, J. Milano, and M. Gensch, Appl. Phys. Lett. **112**, 252404 (2018).
[38] N. Kida, Y. Takahashi, J. S. Lee, R. Shimano, Y. Yamasaki, Y. Kaneko, S. Miyahara, N. Furukawa, T. Arima, and Y. Tokura, J. Opt. Soc. Am. B **26**, A35 (2009).
[39] X. Fu, X. Zeng, D. Wang, H. C. Zhang, J. Han, and T. J. Cui, Sci. Rep. **5**, 14777 (2015).
[40] Y. Takahashi, Y. Yamasaki, and Y. Tokura, Phys. Rev. Lett. **111**, 037204 (2013).
[41] S. Bordács, I. Kézsmárki, D. Szaller, L. Demkó, N. Kida, Y. Onose, R. Shimano, T. Rõõm, U. Nagel, S. Miyahara, N. Furukawa, and Y. Tokura, Nat. Phys **8**, 734 (2012).
[42] A. Zheludev, T. Sato, T. Masuda, K. Uchinokura, G. Shirane, and B. Roessli, Phys. Rev. B **68**, 024428 (2003).
[43] N. Kida and M. Tonouchi, Phys. Rev. B **66**, 024401 (2002).
[44] I. Kawayama, K. Kotani, M. Misra, H. Murakami, and M. Tonouchi, Jpn. J. Appl. Phys. **53**, 09PD06 (2014).
[45] S. Yu, C. Dhanasekhar, V. Adyam, S. Deckoff-Jones, M. K. L. Man, J. Madéo, E. L. Wong, T. Harada, M. B. Murali Krishna, K. M. Dani, and D. Talbayev, Phys. Rev. B **96**, 094421 (2017).
[46] S. Baierl, J. H. Mentink, M. Hohenleutner, L. Braun, T.-M. Do, C. Lange, A. Sell, M. Fiebig, G. Woltersdorf, T. Kampfrath, and R. Huber, Phys. Rev. Lett. **117**, 197201 (2016).
[47] S. Schlauderer, C. Lange, S. Baierl, T. Ebnet, C. P. Schmid, D. C. Valovcin, A. K. Zvezdin, A. V. Kimel, R. V. Mikhaylovskiy, and R. Huber, Nature (London) **569**, 383 (2019).
[48] R. V. Mikhaylovskiy, T. J. Huisman, R. V. Pisarev, Th. Rasing, and A. V. Kimel, Phys. Rev. Lett. **118**, 017205 (2017).
[49] S. Baierl, M. Hohenleutner, T. Kampfrath, A. K. Zvezdin, A. V. Kimel, R. Huber, and R. V. Mikhaylovskiy, Nat. Photon. **10**, 715 (2016).
[50] A. Pimenov, A. A. Mukhin, V. Yu. Ivanov, V. D. Travkin, A. M. Balbashov, and A. Loidl, Nat. Phys. **2**, 97 (2006).
[51] S. Skiadopoulou, F. Borodavka, C. Kadlec, F. Kadlec, M. Retuerto, Z. Deng, M. Greenblatt, and S. Kamba, Phys. Rev. B **95**, 184435 (2017).
[52] N. Kida, D. Okuyama,S. Ishiwata, Y. Taguchi, R. Shimano, K. Iwasa, T. Arima, and Y. Tokura, Phys. Rev. B **80**, 220406(R) (2009).
[53] C. M. Morris, R. Valdés Aguilar, A. Ghosh, S. M. Koohpayeh, J. Krizan, R. J. Cava, O. Tchernyshyov, T. M. McQueen, and N. P. Armitage, Phys. Rev. Lett. **112**, 137403 (2014).
[54] A. Legros, S.-S. Zhang, X. Bai, H. Zhang, Z. Dun, W. A. Phelan, C. D. Batista, M. Mourigal, and N. P. Armitage, Phys. Rev. Lett. **127**, 267201 (2021).